

Controllable photocurrent generation in Dirac systems with two frequency drives

Yuya Ikeda, Sota Kitamura, and Takahiro Morimoto

Department of Applied Physics, The University of Tokyo, Hongo, Tokyo, 113-8656, Japan

(Dated: June 24, 2024)

We study the bulk photovoltaic effect (BPVE) in Dirac and Weyl semimetals under two-frequency light irradiation. We show that the BPVE emerges for centrosymmetric Dirac and Weyl semimetals in the presence of light fields with frequencies Ω and 2Ω . The BPVE under the two frequency drive involves both shift current contribution independent of the carriers lifetime τ and the injection current contribution $\propto \tau$. Our calculations indicate that the photocurrent's direction, magnitude and type can be dynamically controlled by tuning parameters of the driving fields. Furthermore, we find that the tilt of the Dirac cone significantly affects the photocurrent, particularly in mirror symmetry-lacking Weyl semimetals, leading to an anisotropic optical response. These findings provide new insights into the dynamic control of photocurrents in topological semimetals, offering promising applications for optoelectronic devices.

I. INTRODUCTION

The bulk photovoltaic effect (BPVE) [1] is a phenomenon where the light irradiation induces photocurrents in the bulk materials. The BPVE is of fundamental importance in understanding the optoelectronic behavior of noncentrosymmetric materials, and is also essential for application purposes including photodetectors and solar cells [2–4]. The BPVE is in sharp contrast to conventional photovoltaic effects in p-n junction, where the heterostructure is crucial for dissociating photocarriers with the internal electric field. The main mechanisms for the BPVE are the second-order optical response, which can be divided into the injection current, the shift current, and ballistic current [5–7]. The injection current arises from the asymmetric photoexcitation in k -space, while the shift current is due to the shift of the spatial position of the electron wave packet during photoexcitation. The ballistic current is induced by scattering of photocarriers with impurities or phonons and usually depends on the relaxation time of photocarriers. The presence of inversion symmetry \mathcal{P} prohibits the BPVE, while time reversal symmetry \mathcal{T} or \mathcal{PT} symmetry plays an important role in determining which type of photocurrent is generated. For instance, the presence of \mathcal{T} (\mathcal{PT}) symmetry prohibits (allows) the injection currents induced by irradiation of linear polarized light.

Dirac and Weyl systems have attracted a keen attention because of their unique electronic properties characterized by the gapless linear dispersion [8]. These systems are exemplified by 3D Dirac semimetals such as Cd_3As_2 [9, 10] and Na_3Bi [11], as well as by 2D materials like graphene [12], and surface states of topological insulators [13]. The gapless nature of their energy spectra leads to a variety of intriguing phenomena, including high mobility of charge carriers [9], unusual magnetic responses such as chiral anomaly and chiral magnetic effect [14–16]. Inversion-broken Weyl systems also support nonlinear optical effects such as BPVEs [17–19] and quantized circular photogalvanic effect (CPGE) that arises from the Berry curvature of Weyl points [20]. Magnetic Dirac systems, where inversion symmetry \mathcal{P} is broken while \mathcal{PT} is preserved, also support a BPVE [19].

The (standard) monochromatic light-induced BPVE manifests only in materials lacking inversion symmetry. If the BPVE could be achieved even in systems with inversion

symmetry, photocurrent generation would also occur in centrosymmetric Dirac and Weyl systems, leading to novel optical phenomena. Previous studies have revealed that two-frequency drive, where light of frequencies Ω and 2Ω is simultaneously incident on a material, can induce third-order photocurrents even in systems with spatial inversion symmetry [21–24] [See Fig. 1(a)]. The two-frequency drive possesses dynamical symmetries that are absent in single-frequency irradiation [25]. For example, the counter-rotating BCL possesses the dynamical C_3 symmetry in its electric field pattern, which is experimentally demonstrated [26, 27]. Such dynamical symmetries of the incident light enables the dynamical control of the symmetry and topology of materials, providing a powerful tool for manipulating electronic and optical properties [28–35]. Previously, third-order photocurrents have been studied mainly from the perspective of the coherent control induced by quantum interference between one- and two-photon absorption processes [21, 22, 36–39]. However, these studies focused mainly on the injection current contribution proportional to the relaxation time τ , leaving the shift contribution (independent of τ) induced by two-frequency drive unexplored. A comprehensive understanding of the differences between photocurrents generated by monochromatic light and those induced by two-frequency light irradiation is essential. In particular, a systematic analysis of both the injection ($\propto \tau$) and shift ($\propto \tau^0$) contributions in two frequency drives is still missing, and their photocurrent generation in the topological gapless semimetals is an important issue in exploring the future application of two-frequency light.

In this paper, we perform a systematic analysis of the BPVE in Dirac and Weyl systems under two-frequency light irradiation using the diagrammatic technique. First, we provide a detailed diagrammatic framework for the generation of third-order photocurrents in Dirac and Weyl systems under two-frequency drives in Sec. II. We derive the analytical expressions for both third-order injection and shift current conductivities in 3D and 2D Dirac/Weyl systems in Sec. III, showing that a nonmagnetic Dirac and Weyl systems with inversion symmetry \mathcal{P} generally support photocurrents under a two frequency drive. The effect of the tilt of the Dirac cone on the optical third-order conductivities is also discussed analytically. We analytically demonstrate the components of the photocurrent for pairs of circularly or elliptically polarized

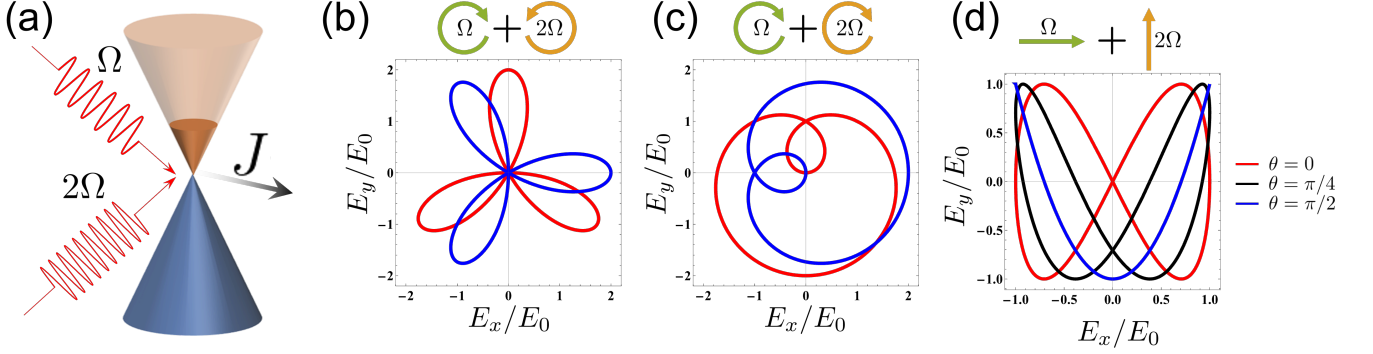


FIG. 1. (a) A schematic picture of the third-order dc photocurrent generation in Dirac electron systems. (b-d) Patterns of electric fields of the two-frequency drive with relative phases $\theta = 0$ (red), $\pi/4$ (black), and $\pi/2$ (blue), for (b) counter-rotating circularly polarized light, (c) co-rotating circularly polarized light, and (d) linearly polarized light.

lights (bicircular light) and linearly polarized lights (bilinear light) in Sec. IV. We found that by tuning the parameters of the incident light, we can not only control the magnitude and direction of the photocurrent but also manipulate the type of photocurrent and achieve directional response separation. Moreover, it is revealed that these photocurrents exhibit low-frequency divergence, which is even more pronounced than the low-frequency divergence in second-order photocurrents in inversion-broken Weyl systems. These behaviors are understood by the symmetry consideration and the dimensional analysis in Sec. V. Finally we perform an order estimation of the photocurrent in the Dirac/Weyl materials in Sec. VI, which indicates the two frequency drive's potential for high-efficiency optoelectronic applications.

II. FORMALISM

In this section, we present our setup of the Bloch electrons in solids that are subjected to the two-frequency driving. We then give a description of the diagrammatic framework to study the two-frequency driving.

A. Two-frequency drive

We consider Bloch electrons in solids that are subjected to the two-frequency drive and are described by the time-dependent Hamiltonian

$$H(t) = H_0(\mathbf{k} + e\mathbf{A}(t)/\hbar), \quad (1)$$

where $H_0(\mathbf{k})$ is the unperturbed Bloch Hamiltonian in the equilibrium. Here we write the charge of an electron as $-e$ with $e > 0$. $\mathbf{A}(t)$ is the vector potential of the two-frequency drive. The electric field is given by

$$\mathbf{E}(t) = -\frac{\partial \mathbf{A}(t)}{\partial t} \equiv \text{Re}[\mathbf{E}^{(\Omega)} e^{i\Omega t} + \mathbf{E}^{(-2\Omega)} e^{-2i\Omega t}], \quad (2)$$

with the complex electric field amplitude $\mathbf{E}^{(\Omega)}$ and $\mathbf{E}^{(-2\Omega)}$. The complex field amplitude can take any value; for example, when illuminated on the x - y plane, circularly or elliptically polarized light with an ellipticity ε corresponds to $(E_x^{(\Omega)}, E_y^{(\Omega)}) \propto (i, \varepsilon)$, while linearly polarized light (LPL) corresponds to $(E_x^{(\Omega)}, E_y^{(\Omega)}) \propto (\cos \phi, \sin \phi)$. Various two-frequency drive are realized by combining the parameters of the two light waves, ε or ϕ . For example, in the case of the counter-rotating bicircular light, the electric field amplitude can be written as

$$\begin{pmatrix} E_x(t) \\ E_y(t) \end{pmatrix} = E_0 \begin{pmatrix} -\sin \Omega t + \sin(2\Omega t - \theta) \\ \cos \Omega t + \cos(2\Omega t - \theta) \end{pmatrix}, \quad (3)$$

where θ represents the phase difference of the two-frequency drive. As shown in Fig. 1(b), the light pattern draws a rose-like shape with three-fold rotational symmetry. On the other hand, the co-rotating bicircular light draws a pattern without rotational symmetry as depicted in Fig. 1(c).

Not only the type of polarization, but also the phase difference of the two-color beams can significantly alter the patterns of two-frequency fields. As shown in Figs. 1(b) and (c), for the case of the two-frequency drive consisting of two circularly polarized lights, the phase difference θ acts like a knob that rotates the field pattern in the two-dimensional plane. On the other hand, for the case of linearly polarized light in Fig. 1(d), changing the phase θ alters the shape of the field pattern itself, rather than just rotating it. This versatility in controlling the direction or shape of the two-frequency electric field through the relative phase θ will have important consequences for the photocurrent response, as we will see later.

B. Diagrammatic framework

In this subsection, we derive the third-order nonlinear dc conductivities defined by

$$J_{\text{dc}}^{\mu} = \sum_{\alpha\beta\gamma} \text{Re}[\sigma^{\mu\alpha\beta\gamma}(0; \Omega, \Omega, -2\Omega) E_{\alpha}^{(\Omega)} E_{\beta}^{(\Omega)} E_{\gamma}^{(-2\Omega)}] \quad (4)$$

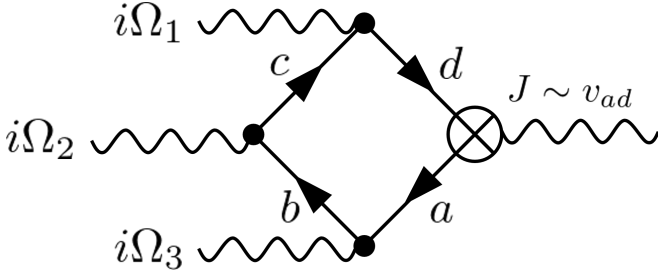


FIG. 2. The box diagram for the third-order dc generation induced by a two-frequency driving. The energy of the absorbed photons $\{i\Omega_1, i\Omega_2, i\Omega_3\}$ is given by a permutation of $\{\hbar\Omega + i\gamma_0, \hbar\Omega + i\gamma_0, -2\hbar\Omega + i\gamma_0\}$.

in the Dirac/Weyl electron systems. Nonlinear optical conductivities can be obtained by the diagrammatic approach [40]. The photocurrent induced by a two-frequency drive is a third-order response with respect to the electric field at the lowest order since $\Omega + \Omega - 2\Omega = 0$. Since the Dirac system contains only k -linear terms, only the contribution of the box diagram consisting of only one-photon parts remains, as shown

in Fig. 2. We note that diagrams including two-photon, three-photon, and four-photon vertices, which correspond to $\partial_k^2 H_0$, $\partial_k^3 H_0$, and $\partial_k^4 H_0$, vanish in the k -linear Hamiltonians. In the box diagram, four black lines represent the electron propagator $G_a(i\omega) = (i\omega - \epsilon_a)^{-1}$, where ϵ_a is the a -th original band energy of the system and $i\omega$ is the Matsubara frequency. Three black vertices stand for the one-photon inputs and we introduce the relaxation rate γ_0 in the photon energies. The other vertex represents the one-photon output with zero total frequency. From the Feynman rules, the contribution of the box diagram can be written down as

$$\sigma^{\mu\alpha\beta\gamma}(0; \Omega, \Omega, -2\Omega) = \frac{-ie^4}{2\hbar^4\Omega^3} \mathcal{S} \sum_{abcd} \int [d\mathbf{k}] v_{ba}^\alpha v_{cb}^\beta v_{dc}^\gamma v_{ad}^\mu \quad (5)$$

$$\times I_4(\hbar\Omega + i\gamma_0, \hbar\Omega + i\gamma_0, -2\hbar\Omega + i\gamma_0),$$

where $v_{ba}^\alpha = \langle b | \frac{\partial H_0}{\partial k_\alpha} | a \rangle$ represents the matrix element of the velocity operator and \mathcal{S} denotes the summation for all possible permutations of input photons $(\alpha, \Omega), (\beta, \Omega), (\gamma, -2\Omega)$. Also we defined a shorthand notation for the \mathbf{k} integral as $[d\mathbf{k}] \equiv d\mathbf{k}/(2\pi)^d$ with the spatial dimension d . The frequency integral in the box diagram, which we call I_4 , is performed for imaginary-time Green's functions as [40]

$$I_4(i\Omega_1, i\Omega_2, i\Omega_3) = \int \frac{d\omega}{2\pi} G_a(i\omega) G_b(i\omega + i\Omega_1) G_c(i\omega + i\Omega_1 + i\Omega_2) G_d(i\omega + i\Omega_1 + i\Omega_2 + i\Omega_3)$$

$$= \frac{f(\epsilon_a)}{(\epsilon_{ab} + i\Omega_1)(\epsilon_{ac} + i\Omega_{12})(\epsilon_{ad} + i\Omega_{123})} + \frac{f(\epsilon_b)}{(\epsilon_{ba} - i\Omega_1)(\epsilon_{bc} + i\Omega_2)(\epsilon_{bd} + i\Omega_{23})} \quad (6)$$

$$+ \frac{f(\epsilon_c)}{(\epsilon_{ca} - i\Omega_{12})(\epsilon_{cb} - i\Omega_2)(\epsilon_{cd} + i\Omega_3)} + \frac{f(\epsilon_d)}{(\epsilon_{da} - i\Omega_{123})(\epsilon_{db} - i\Omega_{23})(\epsilon_{dc} - i\Omega_3)},$$

where $\epsilon_{ab} = \epsilon_a - \epsilon_b$, $i\Omega_{12} = i\Omega_1 + i\Omega_2$, and $i\Omega_{123} = i\Omega_1 + i\Omega_2 + i\Omega_3$. I_4 in Eq. (5) is obtained after analytic continuation of Matsubara frequencies,

$$i\Omega_1 \rightarrow \hbar\Omega + i\gamma_0, \quad i\Omega_2 \rightarrow \hbar\Omega + i\gamma_0, \quad i\Omega_3 \rightarrow -2\hbar\Omega + i\gamma_0, \quad (7)$$

in the above expression, where γ_0 corresponds to the energy broadening. Note that the Matsubara frequency $i\omega$ is defined such that it has the dimension of the energy.

It is known that the second-order dc generation in non-centrosymmetric materials arises from two mechanisms in the clean limit: the injection current and the shift current. The shift current occurs due to changes of the real space position of the electron during the optical excitation. The injection current is a relaxation process and is proportional to the relaxation time $\tau = \hbar/\gamma_0$, while the shift current is independent of the relaxation time. By focusing on interband transitions in the clean limit, the third-order dc generation can also be divided into two components: the contribution proportional to the relaxation time τ and the one independent of τ , which we call injection and shift contributions in this paper, in a similar manner to the second order responses. Specifically, we

decompose the third order nonlinear conductivity as

$$\sigma_{dc} = \sigma_1 + \sigma_0 + \mathcal{O}(\gamma_0) \quad (\gamma_0 \rightarrow 0), \quad (8)$$

with $\sigma_{dc} = \sigma(0; \Omega, \Omega, -2\Omega)$, where the two conductivities $\sigma_i \propto \tau^i$ (injection: $i = 1$, shift: $i = 0$) are defined as

$$\sigma_1 = \frac{1}{\gamma_0} \lim_{\gamma_0 \rightarrow 0} \gamma_0 \sigma_{dc}, \quad (9)$$

$$\sigma_0 = \lim_{\gamma_0 \rightarrow 0} (\sigma_{dc} - \sigma_1). \quad (10)$$

Note that the shift conductivity σ_0 in the third order case does not necessarily correspond to contributions to current generation arising from a real space shift of the electron wave packet as in the second order case. From the above expressions, we can obtain the following general formulas for two-band mod-

els, for example,

$$\sigma_1^{xxxx} = \frac{-2ie^4}{3\gamma_0\hbar^5\Omega^4} \int [d\mathbf{k}] |v_{12}^x|^2 (\Delta^x)^2 \times \left(\frac{1}{2} \delta(\epsilon_{12} + \hbar\Omega) - \delta(\epsilon_{12} + 2\hbar\Omega) \right), \quad (11)$$

$$\sigma_0^{xxxx} = \frac{-e^4}{3\hbar^6\Omega^5} \int [d\mathbf{k}] |v_{12}^x|^2 [24|v_{12}^x|^2 - (\Delta^x)^2] \times \left(\frac{1}{2} \delta(\epsilon_{12} + \hbar\Omega) - \delta(\epsilon_{12} + 2\hbar\Omega) \right), \quad (12)$$

where $\Delta^x = v_{11}^x - v_{22}^x$ is the difference of the velocity between the valence and conduction band. We can see that the photocurrent induced by two-frequency driving involves two interband resonance terms: the Ω -resonant term $\propto \delta(\epsilon_{12} + \hbar\Omega)$ and the 2Ω -resonant term $\propto \delta(\epsilon_{12} + 2\hbar\Omega)$ with a sign change.

III. OPTICAL CONDUCTIVITY IN DIRAC SYSTEMS

A. 3D Dirac/Weyl electrons

We focus on the photocurrent generation induced by two-frequency drives for Dirac/Weyl semimetals, which are characterized by their gapless linear dispersion. We first consider a 3D model representing a Weyl fermion with an anisotropy in velocity along the z direction, which is given by the Hamiltonian,

$$H^{3D} = \hbar v_F (k_x \sigma_x + k_y \sigma_y + \eta k_z \sigma_z). \quad (13)$$

Here v_F is a Fermi velocity and η denotes the anisotropy along the z direction.

Let us consider the third-order dc conductivities in this 3D Dirac model. Because of C_2^i ($i = x, y, z$) symmetry and the SO(2) rotational symmetry around the z -axis in the Weyl Hamiltonian as in Eq. (13), there are only eight independent components,

$$\begin{aligned} & \sigma^{xxxx}, \quad \sigma^{xxzz}, \quad \sigma^{xzxz}, \quad \sigma^{xzzx}, \\ & \sigma^{zzzz}, \quad \sigma^{zzxx}, \quad \sigma^{zxzx}, \quad \sigma^{zxzx}. \end{aligned} \quad (14)$$

Since SO(2) symmetry around the z -axis is imposed, only two-dimensional components remain, and three-dimensional components such as σ^{xyz} disappear. The other components obtained by replacing x with y in Eq. (14) are the same as before the replacement; e.g., $\sigma^{xyz} = \sigma^{xyx}$. The components obtained by replacing z with y in Eq. (14) can be obtained by substituting $\eta = 1$. We note that the presence of a tilt of the Dirac cone lowers the symmetry of the Dirac cone and leads to additional components, which we discuss in Sec. III C.

By incorporating a variable change as $(k_x, k_y, k_z) = k(\sin \varphi \cos \psi, \sin \varphi \sin \psi, \cos \varphi/\eta)$, we can perform the k -integration analytically to compute the injection and shift con-

ductivities as

$$\begin{pmatrix} \sigma_1^{xxxx} \\ \sigma_1^{xxzz} \\ \sigma_1^{xzxz} \\ \sigma_1^{xzzx} \end{pmatrix} = \frac{-4ie^4 |v_F| \Theta_0}{45\pi\gamma_0 \hbar^2 \Omega^2 |\eta|} \begin{pmatrix} 1 \\ 2\eta^2 \\ 2\eta^2 \\ -3\eta^2 \end{pmatrix}, \quad \begin{pmatrix} \sigma_1^{zzzz} \\ \sigma_1^{zzxx} \\ \sigma_1^{zxzx} \\ \sigma_1^{zxzx} \end{pmatrix} = \frac{-4ie^4 |v_F| \Theta_0}{45\pi\gamma_0 \hbar^2 \Omega^2 |\eta|} \begin{pmatrix} \eta^4 \\ 2\eta^2 \\ 2\eta^2 \\ -3\eta^2 \end{pmatrix}, \quad (15)$$

$$\begin{pmatrix} \sigma_0^{xxxx} \\ \sigma_0^{xxzz} \\ \sigma_0^{xzxz} \\ \sigma_0^{xzzx} \end{pmatrix} = \frac{-2e^4 |v_F| \Theta_0}{45\pi\hbar^3 \Omega^3 |\eta|} \begin{pmatrix} 23 \\ 16\eta^2 \\ 16\eta^2 \\ -9\eta^2 \end{pmatrix}, \quad \begin{pmatrix} \sigma_0^{zzzz} \\ \sigma_0^{zzxx} \\ \sigma_0^{zxzx} \\ \sigma_0^{zxzx} \end{pmatrix} = \frac{-2e^4 |v_F| \Theta_0}{45\pi\hbar^3 \Omega^3 |\eta|} \begin{pmatrix} 23\eta^4 \\ 16\eta^2 \\ 16\eta^2 \\ -9\eta^2 \end{pmatrix}. \quad (16)$$

Here the symbol $\Theta_0 = \Theta(\hbar\Omega - 2\epsilon_F)/8 - \Theta(\hbar\Omega - \epsilon_F)$ with the step function $\Theta(x)$ represents the condition for the optical excitation within Dirac cones. This shows that the injection conductivities are purely imaginary, whereas the shift conductivities are real. This distinction is attributed to the difference in whether $3i\gamma_0$ is picked up from the energy denominator I_4 [see Eq. (6)].

B. 2D Dirac electrons

Next, we turn our focus toward two-dimensional Dirac electron systems represented by

$$H^{2D} = \hbar v_F (k_x \sigma_x + \eta k_y \sigma_y) + m \sigma_z, \quad (17)$$

This Hamiltonian describes, for example, the Dirac surface states of a topological insulator or the Dirac fermions in graphene with valley and spin degeneracy. In the massless case ($m = 0$), we obtain

$$\begin{pmatrix} \sigma_1^{xxxx} \\ \sigma_1^{kxyx} \\ \sigma_1^{kyxy} \\ \sigma_1^{kyyx} \end{pmatrix} = \frac{-ie^4 v_F^2 \Theta'_0}{12\gamma_0 \hbar^2 \Omega^3 |\eta|} \begin{pmatrix} 1 \\ 3\eta^2 \\ 3\eta^2 \\ -5\eta^2 \end{pmatrix}, \quad \begin{pmatrix} \sigma_1^{yyyy} \\ \sigma_1^{lyxx} \\ \sigma_1^{lyyx} \\ \sigma_1^{lyxy} \end{pmatrix} = \frac{-ie^4 v_F^2 \Theta'_0}{12\gamma_0 \hbar^2 \Omega^3 |\eta|} \begin{pmatrix} \eta^4 \\ 3\eta^2 \\ 3\eta^2 \\ -5\eta^2 \end{pmatrix}, \quad (18)$$

$$\begin{pmatrix} \sigma_0^{xxxx} \\ \sigma_0^{kxyx} \\ \sigma_0^{kyxy} \\ \sigma_0^{kyyx} \end{pmatrix} = \frac{-e^4 v_F^2 \Theta'_0}{24\hbar^3 \Omega^4 |\eta|} \begin{pmatrix} 17 \\ 3\eta^2 \\ 3\eta^2 \\ 11\eta^2 \end{pmatrix}, \quad \begin{pmatrix} \sigma_0^{yyyy} \\ \sigma_0^{lyxx} \\ \sigma_0^{lyyx} \\ \sigma_0^{lyxy} \end{pmatrix} = \frac{-e^4 v_F^2 \Theta'_0}{24\hbar^3 \Omega^4 |\eta|} \begin{pmatrix} 17\eta^4 \\ 3\eta^2 \\ 3\eta^2 \\ 11\eta^2 \end{pmatrix}, \quad (19)$$

where $\Theta'_0 = \Theta(\hbar\Omega - 2\epsilon_F)/4 - \Theta(\hbar\Omega - \epsilon_F)$. The other components vanish identically. As in the 3D massless Dirac case, eight nonzero conductivities have been identified from symmetry considerations.

For the massive case ($m \neq 0$), we find the effect of the mass gap on the optical conductivities,

$$\sigma_1^{xxxx} = \frac{-ie^4 v_F^2}{12\gamma_0 \hbar^2 \Omega^3 |\eta|} \left[\frac{1}{4} g_1^{xxxx} \left(\frac{2m}{\hbar\Omega}, \frac{2\epsilon_F}{\hbar\Omega} \right) - g_1^{xxxx} \left(\frac{m}{\hbar\Omega}, \frac{\epsilon_F}{\hbar\Omega} \right) \right], \quad (20)$$

where

$$g_1^{xxxx}(x, y) = \Theta(1-x)\Theta(1-y)(1+2x^2-3x^4) \quad (21)$$

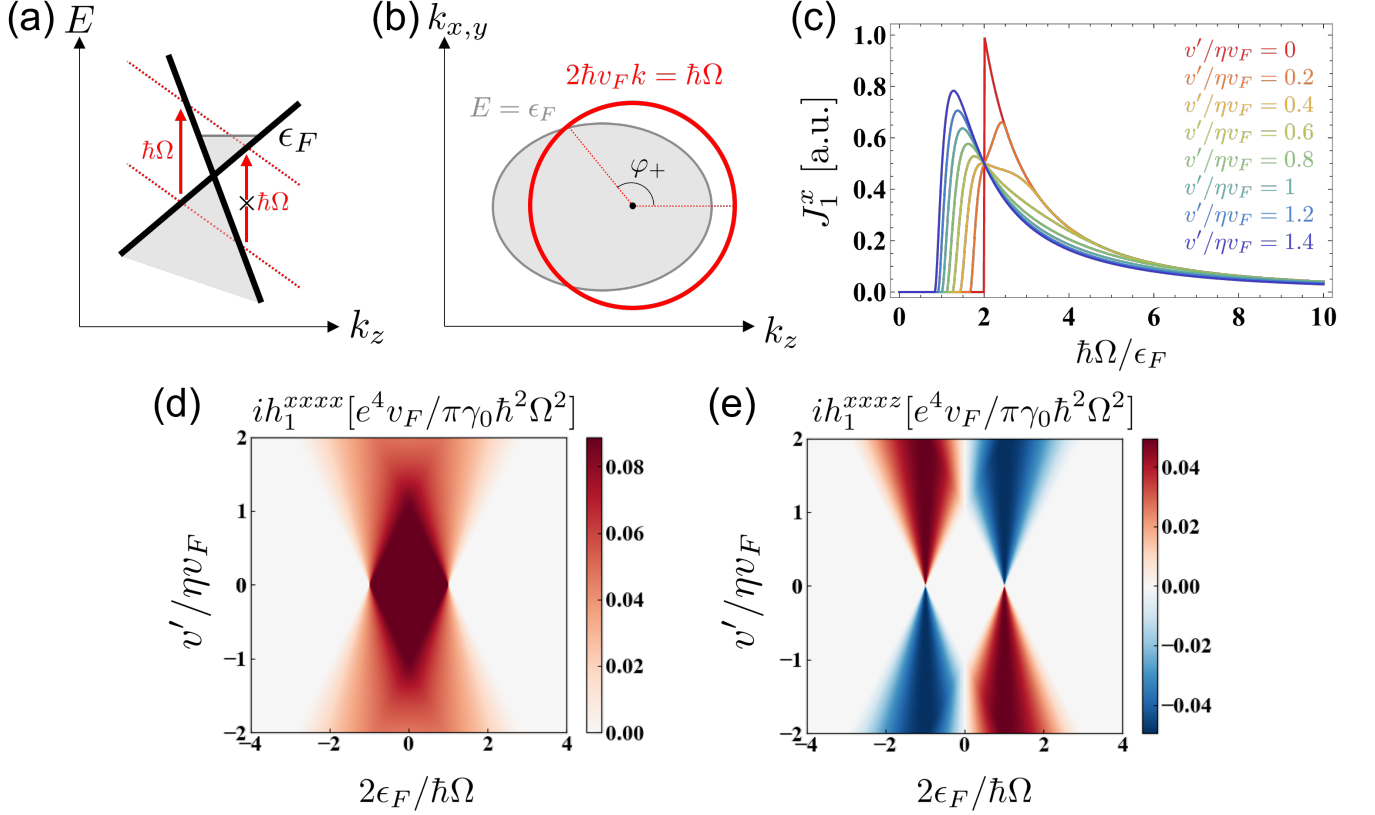


FIG. 3. Third order dc conductivities in tilted 3D Dirac electron systems. (a) Schematic illustration of the anisotropic optical transitions in a tilted Dirac cone system. (b) The red circle represents the surface of the resonance condition $\epsilon_{l2} = \hbar\Omega$. The gray area shows the Fermi surface. The Fermi surface is distorted by the tilt, and the optical transition can occur only for a part of the red circle outside the gray area due to the Pauli blocking. (c) Frequency dependence of the photocurrent for various tilt strengths with $\eta = 1/4$. As the tilt increases, the peak shifts towards lower frequencies as optical transitions become possible even for $\hbar\omega < 2\epsilon_F$. (d,e) Density plots of the function $h = \mathcal{F}(\varphi_+) - \mathcal{F}(\varphi_-)$, which characterizes the photocurrent, as a function of tilt strength and frequency. Panel (d) shows the term ih_1^{xxxx} that exists even without tilt, while panel (e) shows the term ih_1^{xxxz} induced by the tilt.

is a function that takes the ratio of the input frequency to the mass and Fermi level as arguments. g_0^{xxxx} contains essential information on the conditions for optical excitations, and is always positive. One can immediately see that this is consistent with the case $m = 0$. Due to the breaking of mirror symmetries M_x, M_y induced by the mass term m , the other conductivity components, e.g. σ^{xxy} , can be finite as

$$\sigma_1^{xxy} = \frac{2e^4 v_F^2 \text{sgn}(\eta)}{3\gamma_0 \hbar^2 \Omega^3} \left[\frac{1}{4} g_1^{xxy} \left(\frac{2m}{\hbar\Omega}, \frac{2\epsilon_F}{\hbar\Omega} \right) - g_1^{xxy} \left(\frac{m}{\hbar\Omega}, \frac{\epsilon_F}{\hbar\Omega} \right) \right], \quad (22)$$

with $g_1^{xxy}(x, y) = \Theta(1-x)\Theta(1-y)(x-x^3)$. The m -induced injection (shift) conductivities are real (purely imaginary), while the other injection (shift) conductivities are purely imaginary (real). In addition, these conductivities are characterized by dependence on the chirality of the Dirac cone, i.e. $\text{sgn}(\eta)$.

C. Effect of the tilt

In this section, we discuss the effect of tilt on the dc conductivities. The tilt of the dispersion causes optical excitation to be anisotropic around the Dirac point in the k -space due to the Pauli blocking (rather than occurring on the full sphere around the Dirac point) as shown schematically in Figs. 3(a,b), whose consequence was discussed in the case of second order optical conductivity [17, 20]. Here we consider a 3D Dirac electron with a tilt along the z -axis that is described by

$$H_{\text{tilt}}^{\text{3D}} = \hbar v' k_z \sigma_0 + \hbar v_F (k_x \sigma_x + k_y \sigma_y + \eta k_z \sigma_z), \quad (23)$$

where v' represents the overall velocity shift due to the tilt. The Dirac fermion described by this Hamiltonian is called type-I when $|v'/v_F| < 1$ and type-II when $|v'/v_F| > 1$ [41].

The dc conductivities can be expressed in the form

$$\sigma^{\mu\alpha\beta\gamma} = \frac{1}{8} h^{\mu\alpha\beta\gamma} \left(\frac{v'}{\eta v_F}, \frac{2\epsilon_F}{\hbar\Omega} \right) - h^{\mu\alpha\beta\gamma} \left(\frac{v'}{\eta v_F}, \frac{\epsilon_F}{\hbar\Omega} \right), \quad (24)$$

$$h^{\mu\alpha\beta\gamma}(x, y) = \mathcal{F}^{\mu\alpha\beta\gamma}(\varphi_+) - \mathcal{F}^{\mu\alpha\beta\gamma}(\varphi_-). \quad (25)$$

Here, the function \mathcal{F} is obtained as an indefinite integral with respect to φ in the k -integration Eq. (5). For example, the component \mathcal{F}_1^{xxxx} [defined by $\mathcal{F} = \mathcal{F}_1 + \mathcal{F}_0 + \mathcal{O}(\gamma_0)$ as in Eq. (8)] is given by

$$\mathcal{F}_1^{xxxx}(\varphi) = \frac{-ie^4|v_F|}{5760\pi\gamma_0\hbar^2\Omega^2|\eta|}(-270\cos\varphi + 5\cos 3\varphi + 9\cos 5\varphi). \quad (26)$$

φ_+ and φ_- are the maximum and minimum φ that satisfies

$$|x\cos\varphi - y| < 1, \quad (27)$$

which means the condition that only the lower band is occupied and optical excitation occurs with $(k_x, k_y, k_z) = k(\sin\varphi\cos\psi, \sin\varphi\sin\psi, \cos\varphi/\eta)$ [See Fig. 3(b)]. Note that the dc conductivities without the tilt [Eq. (15)] can be recovered by substituting $\varphi_+ = \pi$ and $\varphi_- = 0$ into the above expression. Introducing a nonzero tilt for the Dirac cone makes the optical transitions anisotropic in the k space and broadens the frequency range of the optical transition, where the lower bound of the allowed frequency for the optical transition is given by

$$\hbar\Omega_{\min} = \frac{2\epsilon_F}{1 + v'/\eta v_F}. \quad (28)$$

This leads to a shift of the frequency peak towards lower frequencies, as shown in Fig 3(c).

The presence of the tilt breaks the mirror symmetry M_z , and allows the emergence of additional components other than the eight conductivity tensor components listed in Eq. (14). While the remaining SO(2) symmetry around the z -axis prohibits the three dimensional components, the following eight tensor components appear due to the tilt as

$$\begin{matrix} \sigma^{xxz}, & \sigma^{xxz}, & \sigma^{yzx}, & \sigma^{xzz}, \\ \sigma^{zzx}, & \sigma^{zzx}, & \sigma^{zxx}, & \sigma^{zxx}. \end{matrix} \quad (29)$$

For example, we obtain

$$\mathcal{F}_1^{xxz}(\varphi) = \frac{-2ie^4|v_F|\text{sgn}(\eta)}{45\pi^2\gamma_0\hbar^2\Omega^2}(-6 + \cos 2\varphi)\sin^3\varphi. \quad (30)$$

Again, the dc conductivity at zero tilting vanishes because $\mathcal{F}_1^{xxz}(\pi) - \mathcal{F}_1^{xxz}(0) = 0$. Unlike the massive 2D Dirac case, \mathcal{F}_1^{xxxx} and \mathcal{F}_1^{xxz} are both purely imaginary because the additional components induced by the tilt originate from anisotropic optical excitations in k -space.

As representative 3D Dirac semimetals, we can consider Dirac materials such as Cd₃As₂ and Na₃Bi, which host two Dirac cones [9–11]. These two cones are connected by the mirror symmetry M_z of the crystal, and they possess opposite signs of tilt. The reversed tilt slope, $v' \rightarrow -v'$, corresponds to the angle transformation $(\varphi_+, \varphi_-) \rightarrow (\pi - \varphi_-, \pi - \varphi_+)$, which is equivalent to reversing the Fermi level $\epsilon_F \rightarrow -\epsilon_F$ as seen from Eq. (27). The original tensor components [Eq. (14)] satisfy $\mathcal{F}(\pi - \varphi) = -\mathcal{F}(\varphi)$, whereas the additional terms induced by the tilt [Eq. (29)] satisfy $\mathcal{F}(\pi - \varphi) = \mathcal{F}(\varphi)$. Consequently, the original components fulfill the relationship

$h^{\mu\alpha\beta\gamma}(-x, y) = h^{\mu\alpha\beta\gamma}(x, -y) = h^{\mu\alpha\beta\gamma}(x, y)$, while the additional components fulfill $h^{\mu\alpha\beta\gamma}(-x, y) = h^{\mu\alpha\beta\gamma}(x, -y) = -h^{\mu\alpha\beta\gamma}(x, y)$ [see Figs. 3(d,e)]. Therefore, in tilted Dirac systems where the crystal hosts mirror symmetry as a whole, the additional components induced by the tilt turn out to cancel out for two Dirac cones. This is also understandable from the symmetry and tensor component arguments discussed previously. However, if one examines lower symmetric Weyl systems [42, 43], it will become possible to measure the tilt-induced contributions to the photocurrent induced by the two-frequency drive.

IV. PHOTOCURRENT UNDER TWO-FREQUENCY DRIVE

Since the third-order nonlinear dc conductivities are derived analytically in the previous section, we obtain the photocurrent simply by multiplying the complex amplitude of the two-frequency drive as

$$J_1^\mu(\Omega) = \sum_{\alpha\beta\gamma} \text{Re}[\sigma_1^{\mu\alpha\beta\gamma} E_\alpha^{(\Omega)} E_\beta^{(\Omega)} E_\gamma^{(-2\Omega)}], \quad (31)$$

$$J_0^\mu(\Omega) = \sum_{\alpha\beta\gamma} \text{Re}[\sigma_0^{\mu\alpha\beta\gamma} E_\alpha^{(\Omega)} E_\beta^{(\Omega)} E_\gamma^{(-2\Omega)}]. \quad (32)$$

In this section, we demonstrate how we can dynamically control the photocurrent by tuning the parameters of the incident light.

A. Circular polarization

Let us consider a two-frequency drive with elliptical polarization of ellipticity ϵ_1, ϵ_2 ,

$$\mathbf{E}^{(\Omega)} = E_0 \begin{pmatrix} i \\ 0 \\ \epsilon_1 \end{pmatrix}, \quad \mathbf{E}^{(-2\Omega)} = E_0 e^{i\theta} \begin{pmatrix} i \\ 0 \\ \epsilon_2 \end{pmatrix}. \quad (33)$$

Each electric field corresponds to circularly polarized for $\epsilon_i = \pm 1$, linearly polarized for $\epsilon_i = 0$, and elliptically polarized for other values. From Eqs. (15,16), we obtain the analytical expression of the photocurrent in the 3D Dirac systems as

$$J_1^x = \frac{4e^4|v_F|\Theta_0 E_0^3}{45\pi\gamma_0\hbar^2\Omega^2|\eta|} \cos\theta [-1 + \epsilon_1(-3\epsilon_1 + 4\epsilon_2)\eta^2], \quad (34)$$

$$J_1^z = \frac{4e^4|v_F|\Theta_0\eta^2 E_0^3}{45\pi\gamma_0\hbar^2\Omega^2|\eta|} \sin\theta [3\epsilon_2 + \epsilon_1(-4 + \epsilon_1\epsilon_2\eta^2)], \quad (35)$$

$$J_0^x = \frac{-2e^4|v_F|\Theta_0 E_0^3}{45\pi\hbar^3\Omega^3|\eta|} \sin\theta [23 + \epsilon_1(9\epsilon_1 - 32\epsilon_2)\eta^2], \quad (36)$$

$$J_0^z = \frac{-2e^4|v_F|\Theta_0\eta^2 E_0^3}{45\pi\hbar^3\Omega^3|\eta|} \cos\theta [9\epsilon_2 + \epsilon_1(-32 + 23\epsilon_1\epsilon_2\eta^2)]. \quad (37)$$

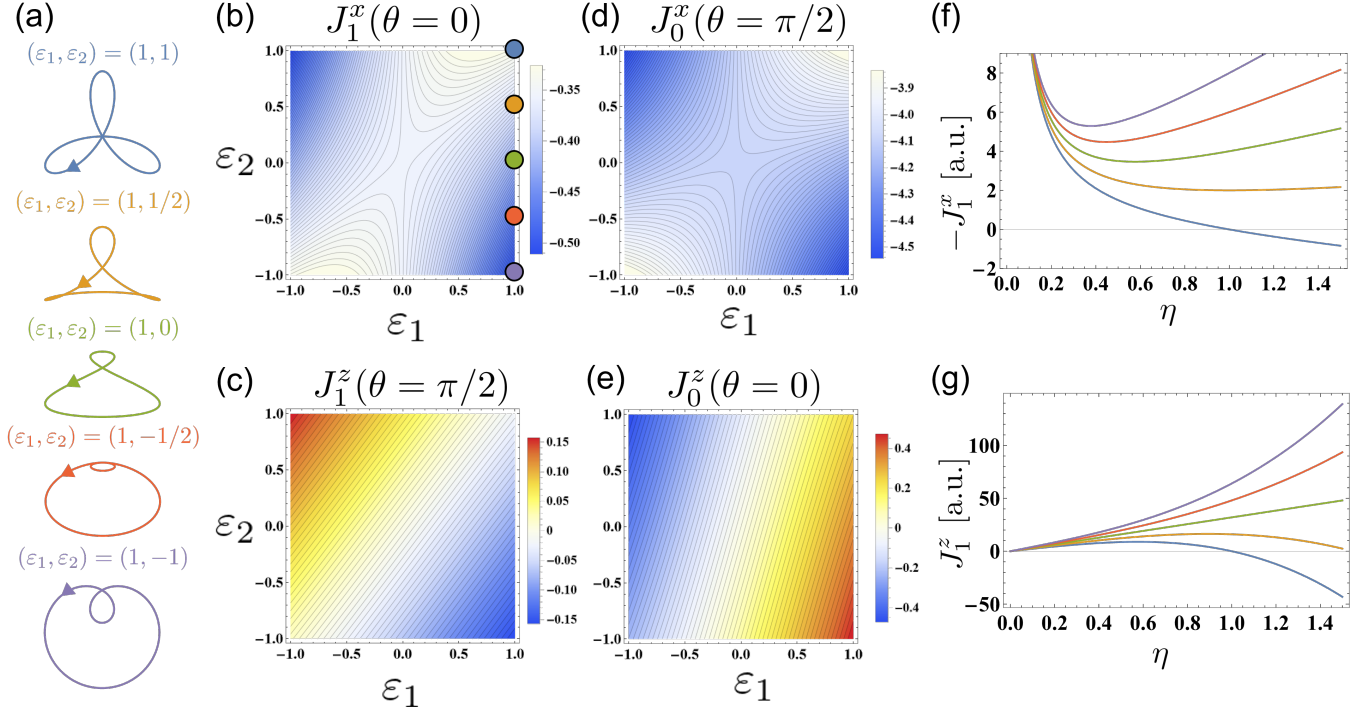


FIG. 4. Photocurrent in 3D Dirac electron systems induced by circularly polarized two-frequency electric fields. (a) Patterns of the circularly polarized two-frequency electric field with different ellipticities $(\varepsilon_1, \varepsilon_2) = (1, 1), (1, 1/2), (1, 0), (1, -1/2), (1, -1)$. (b-e) Color plots of the photocurrent components as a function of the ellipticities ε_1 and ε_2 . The dots in (b) correspond to the patterns of the two-frequency drive shown in (a) with matching colors. The calculations were performed with $\eta = 1/4$, $\theta = 0$ in (b,e) and $\theta = \pi/2$ in (c,d). The units of the photocurrent are given by $[e^4 v_F E_0^3 / \pi \gamma_0 \hbar^2 \Omega^2]$ for J_1 and $[e^4 v_F E_0^3 / \pi \hbar^3 \Omega^3]$ for J_0 . (f,g) Plots of J_1 as a function of the anisotropy η for the five different light patterns shown in (a).

Similarly, from Eqs. (18,19), we obtain the photocurrent in the 2D Dirac system as

$$J_1^x = \frac{e^4 v_F^2 \Theta_0' E_0^3}{12 \gamma_0 \hbar^2 \Omega^3 |\eta|} \cos \theta [-1 + \varepsilon_1 (-5\varepsilon_1 + 6\varepsilon_2) \eta^2], \quad (38)$$

$$J_1^y = \frac{e^4 v_F^2 \Theta_0' \eta^2 E_0^3}{12 \gamma_0 \hbar^2 \Omega^3 |\eta|} \sin \theta [5\varepsilon_2 + \varepsilon_1 (-6 + \varepsilon_1 \varepsilon_2 \eta^2)], \quad (39)$$

$$J_0^x = \frac{-e^4 v_F^2 \Theta_0' E_0^3}{24 \hbar^3 \Omega^4 |\eta|} \sin \theta [17 - \varepsilon_1 (11\varepsilon_1 + 6\varepsilon_2) \eta^2], \quad (40)$$

$$J_0^y = \frac{-e^4 v_F^2 \Theta_0' \eta^2 E_0^3}{24 \hbar^3 \Omega^4 |\eta|} \cos \theta [11\varepsilon_2 + \varepsilon_1 (6 - 17\varepsilon_1 \varepsilon_2 \eta^2)]. \quad (41)$$

This shows that the direction of the two components of the photocurrent can be controlled with the relative phase θ of the two-frequency drive, where the direction of the photocurrent (J_0^x, J_0^y) or (J_1^x, J_1^y) draws an ellipse with an ellipticity that depends on the parameters $\varepsilon_1, \varepsilon_2, \eta$ as the relative phase θ varies. We note that the photocurrent vanishes in the case of the counter-rotating bicircular light, i.e., $(\varepsilon_1, \varepsilon_2) = (1, 1)$, with $\eta \rightarrow 1$ as $(J_1^x, J_1^y) \propto (1 - \eta^2)(\cos \theta, \eta^2 \sin \theta)$ due to the three-fold rotational symmetry of the BCL [23]. Figure 4 shows the color plots of the ellipticity dependence of the four components of the photocurrent in 3D Dirac systems and the anisotropy dependence of the photocurrent for the five

light patterns. The ellipticity significantly affects the magnitude, direction, and material parameter dependence (here the anisotropy η) of the photocurrent. Figures 4(b-e) showing the photocurrent components as a function of the ellipticities ε_1 and ε_2 indicates that the photocurrent in 3D Dirac systems is maximized for co-rotating bicircular light $(\varepsilon_1, \varepsilon_2) = \pm(1, -1)$.

When applying a two-frequency drive with an inverted amplitude in the x direction instead, $E^x \rightarrow -E^x$, only the photocurrent in the x direction is found to be inverted as $(J^x, J^z) \rightarrow (-J^x, J^z)$. This can be simply understood from which components of the conductivity are nonzero as listed in Eq. (14). This phenomenon is similar to the second-order circular photogalvanic effect in time reversal symmetric systems derived from σ_{inj}^{zxy} , but is different in that the current direction is changed (not reversed) in the BCL case.

Another interesting phenomenon is directional separation of shift and injection photocurrent responses. Specifically, J_1^x and J_0^z are proportional to $\cos \theta$, whereas J_1^z and J_0^x are proportional to $\sin \theta$, which is systematically determined by whether corresponding conductivity tensor components are real or purely imaginary. For example, when $\theta = 0$, a directional separation of photocurrent responses occurs such that the injection current and the shift current flows along the x and z directions, respectively. Although such phenomena have been reported in magnetic systems [19], dc response separa-

tion in non-magnetic systems has not been reported to the best of our knowledge.

B. Linear polarization

Next, we consider a two-frequency drive with two linearly polarized light, which is called bilinear light,

$$E^{(\Omega)} = iE_0 \begin{pmatrix} \cos \phi_1 \\ 0 \\ \sin \phi_1 \end{pmatrix}, \quad E^{(-2\Omega)} = iE_0 e^{i\theta} \begin{pmatrix} \cos \phi_2 \\ 0 \\ \sin \phi_2 \end{pmatrix}, \quad (42)$$

where ϕ_i represents the angle of polarization in the x - z plane. In bilinear light case, the photocurrent is given by

$$J_1^x = \frac{-4e^4 |v_F| \Theta_0 E_0^3}{45\pi\gamma_0 \hbar^2 \Omega^2 |\eta|} \cos \theta \left[2\eta^2 \sin 2\phi_1 \sin \phi_2 + (\cos^2 \phi_1 - 3\eta^2 \sin^2 \phi_1) \cos \phi_2 \right], \quad (43)$$

$$J_1^z = \frac{-4e^4 |v_F| \Theta_0 \eta^2 E_0^3}{45\pi\gamma_0 \hbar^2 \Omega^2 |\eta|} \cos \theta \left[2 \sin 2\phi_1 \cos \phi_2 - (3 \cos^2 \phi_1 - \eta^2 \sin^2 \phi_1) \sin \phi_2 \right], \quad (44)$$

$$J_0^x = \frac{-2e^4 |v_F| \Theta_0 E_0^3}{45\pi \hbar^3 \Omega^3 |\eta|} \sin \theta \left[16\eta^2 \sin 2\phi_1 \sin \phi_2 + (23 \cos^2 \phi_1 - 9\eta^2 \sin^2 \phi_1) \cos \phi_2 \right], \quad (45)$$

$$J_0^z = \frac{-2e^4 |v_F| \Theta_0 \eta^2 E_0^3}{45\pi \hbar^3 \Omega^3 |\eta|} \sin \theta \left[16 \sin 2\phi_1 \cos \phi_2 - (9 \cos^2 \phi_1 - 23\eta^2 \sin^2 \phi_1) \sin \phi_2 \right], \quad (46)$$

for the 3D Dirac systems, and

$$J_1^x = \frac{-e^4 v_F^2 \Theta_0' E_0^3}{12\gamma_0 \hbar^2 \Omega^3 |\eta|} \cos \theta \left[3\eta^2 \sin 2\phi_1 \sin \phi_2 + (\cos^2 \phi_1 - 5\eta^2 \sin^2 \phi_1) \cos \phi_2 \right], \quad (47)$$

$$J_1^z = \frac{-e^4 v_F^2 \Theta_0' E_0^3}{12\gamma_0 \hbar^2 \Omega^3 |\eta|} \cos \theta \left[3 \sin 2\phi_1 \cos \phi_2 - (5 \cos^2 \phi_1 - \eta^2 \sin^2 \phi_1) \sin \phi_2 \right], \quad (48)$$

$$J_0^x = \frac{-e^4 v_F^2 \Theta_0' E_0^3}{24\hbar^3 \Omega^4 |\eta|} \sin \theta \left[3\eta^2 \sin 2\phi_1 \sin \phi_2 + (17 \cos^2 \phi_1 + 11\eta^2 \sin^2 \phi_1) \cos \phi_2 \right], \quad (49)$$

$$J_0^z = \frac{-e^4 v_F^2 \Theta_0' E_0^3}{24\hbar^3 \Omega^4 |\eta|} \sin \theta \left[3 \sin 2\phi_1 \cos \phi_2 + (11 \cos^2 \phi_1 + 17\eta^2 \sin^2 \phi_1) \sin \phi_2 \right], \quad (50)$$

for the 2D Dirac systems. Unlike the bicircular light case, the phases of $E_x(t)$ and $E_z(t)$ are aligned for the bilinear light, and the relative phase dependence of the photocurrent is determined only by whether the dc conductivity is real or purely imaginary, which constrains that the injection current is proportional to $\sin \theta$ and the shift current to $\cos \theta$. This indicates

that the type of generated photocurrent can be selected by tuning the relative phase θ of the bilinear light. Such phenomenon does not occur in the second-order dc generation by a monochromatic light.

Furthermore, the magnitude, direction, and η dependence of the photocurrent can also be controlled by tuning the angle of polarization ϕ_1, ϕ_2 for the bilinear light. Figure 5(b-e) shows the color plots of the polarization angle dependence of the photocurrent J_1 and J_0 . The four components of the photocurrent oscillate with respect to the angles ϕ_1 and ϕ_2 . For example, if ϕ_1 is fixed to 0, the injection current draws an ellipse by varying ϕ_2 as $(J_1^x, J_1^z) \propto (\cos \phi_2, -3\eta^2 \sin \phi_2)$ [see Fig. 5(g)]. For other values of ϕ_1 , the trajectory of the current with respect to ϕ_2 in the x - z plane also shows various ellipses centered at the origin, as can be seen from the ϕ_2 dependence of the photocurrent in Eqs. (43-46). Figure 5(f) shows J_1^x as a function of the anisotropy η for several angle pairs, indicating qualitatively different anisotropy dependences of the photocurrent for different light patterns. It can be seen that the polarization angle that maximizes the photocurrent changes radically with the value of the anisotropy of the Dirac cone.

We can consider other particular setups in which two linearly polarized lights are parallel or perpendicular to each other. The photocurrent direction is given by

$$(J^x, J^z) \propto [\cos^2 \phi + \eta^2 \sin^2 \phi](\cos \phi, \eta^2 \sin \phi), \quad (51)$$

for the parallel orientation case ($\phi_1 = \phi_2 = \phi$), and

$$(J_1^x, J_1^z) \propto [1 - 7\eta^2 - (1 - \eta^2) \cos 2\phi](\cos \phi, \eta^2 \sin \phi), \quad (52)$$

for the perpendicular polarization case, $(\phi_1, \phi_2) = (\phi + \pi/2, \phi)$, where the the current directions draw rather complex curves with respect to ϕ and their shapes depend on the anisotropy η . In both cases, we find that the direction and magnitude of the photocurrent can be controlled by tuning the polarization angles.

V. SYMMETRY CONSIDERATION AND DIMENSION ANALYSIS

In this section, we perform a dimensional analysis to study low-frequency divergence of photocurrent under the two-frequency drive. We also perform symmetry consideration for the photocurrent induced by the two-frequency drive.

A. Dimension analysis

Since the Dirac electron system is described by the k linear Hamiltonian and has a scale invariance, the photocurrent response also shows a scale invariance under the change of the frequency $\Omega \rightarrow \lambda\Omega$ as

$$J(\lambda\Omega) = J(\Omega)/\lambda^\Delta, \quad (53)$$

with a scaling dimension Δ . A solution for this scale-invariant photocurrent takes the form

$$J(\Omega) \propto \Omega^{-\Delta} \quad (54)$$

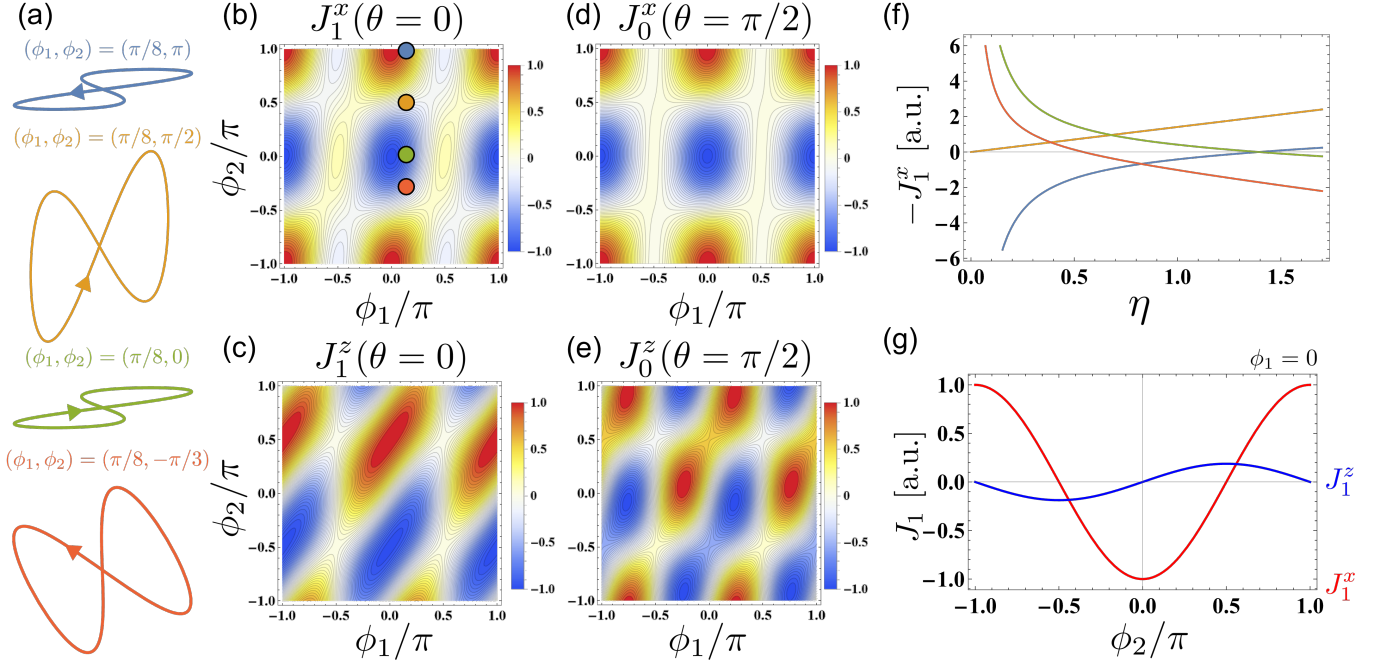


FIG. 5. Photocurrent in 3D Dirac electron systems induced by linearly polarized two-frequency electric fields. (a) Patterns of the linearly polarized two-frequency electric field with different polarization angles $(\phi_1, \phi_2) = (\pi/8, \pi), (\pi/8, \pi/2), (\pi/8, 0), (\pi/8, -\pi/3)$. (b-e) Color plots of the photocurrent components as a function of the polarization angles ϕ_1 and ϕ_2 . The dots in (b) correspond to the patterns of the two-frequency drive shown in (a) with matching colors. The calculations were performed with $\eta = 1/4$, $\theta = 0$ in (b,c) and $\theta = \pi/2$ in (d,e). (f) Plot of J_1 as a function of the anisotropy η for the four different light patterns shown in (a). (g) Plot of J_1 as a function of ϕ_2 with fixing $\phi_1 = 0$, showing that the direction of the photocurrent can be controlled by tuning the polarization angle.

leading to the expressions for J_1 and J_0 as

$$J_1 = C_1 \frac{e^a v_F^b E_0^3}{\hbar^c \gamma_0 \Omega^\Delta}, \quad (55)$$

$$J_0 = C_0 \frac{e^{a'} v_F^{b'} E_0^3}{\hbar^{c'} \Omega^{\Delta'}}, \quad (56)$$

where C_0, C_1 are dimensionless constants including step functions for optical resonance conditions. Since the dimension of the current density for 3D systems and 2D systems is $[A/m^2]$ and $[A/m]$, respectively, a, b, c, Δ are immediately obtained as

$$J_1 = C_1 \frac{e^4 v_F^{4-d} E_0^3}{\hbar^2 \gamma_0 \Omega^{5-d}}, \quad (57)$$

$$J_0 = C_0 \frac{e^4 v_F^{4-d} E_0^3}{\hbar^3 \Omega^{6-d}}. \quad (58)$$

Here, d is the dimension of the system. Note that the dimensionless constants C_0, C_1 are slightly different between 2D and 3D systems.

This dimensional analysis is found to be consistent with the results obtained from the diagrammatic calculations [Eqs. (34-41)]. Furthermore, considering the low-frequency limit, this shows that the photocurrent diverges as $J_1 \propto \Omega^{-(5-d)}$ and $J_0 \propto \Omega^{-(6-d)}$, which can be attributed to the gap-closing dispersion in Dirac/Weyl systems. Additionally, it is clear that the power of the low-frequency divergence is different for J_1 and J_0 , and for the 3D and 2D systems.

B. Symmetry consideration

Next, we consider how the photocurrent change under time reversal operation \mathcal{T} . The general third-order response of the current density J is defined as

$$J(\Omega_{\text{tot}}) = \sigma^{\mu\alpha\beta\gamma}(\Omega_{\text{tot}}; \Omega_1, \Omega_2, \Omega_3) E_\alpha(\Omega_1) E_\beta(\Omega_2) E_\gamma(\Omega_3). \quad (59)$$

Under the time reversal operation \mathcal{T} , the current density transforms as

$$J(\Omega_{\text{tot}}) \xrightarrow{\mathcal{T}} -J(-\Omega_{\text{tot}}), \quad (60)$$

which leads that the third-order photocurrent satisfies

$$J_1 \xrightarrow{\mathcal{T}} J_1, \quad J_0 \xrightarrow{\mathcal{T}} -J_0 \quad (61)$$

for $J_1 \propto 1/\gamma_0$ and $J_0 \propto O((\gamma_0)^0)$, since $\Omega_{\text{tot}} = 3i\gamma_0$ in our setup. On the other hand, the electrical field is converted under \mathcal{T} as

$$E(\Omega_i) \xrightarrow{\mathcal{T}} E(-\Omega_i) = E^*(\Omega_i). \quad (62)$$

In the case of circularly polarized two-frequency electric fields [Eq. (33)], the complex conjugation corresponds to $(E_0, \theta, \varepsilon) \rightarrow (-E_0, -\theta, -\varepsilon)$. Therefore, we can conclude that

J_1 is even and J_0 is odd for the transformation $(\theta, \varepsilon) \rightarrow (-\theta, -\varepsilon)$. This is consistent with the analytical expressions in Eqs. (34-37). Furthermore, Figs. 4(b-e) allow for the verification of the sign of the current with respect to the inversion of the ellipticity. In the case of linearly polarized two-frequency electric fields [Eq. (42)], the complex conjugation corresponds to $(E_0, \theta) \rightarrow (-E_0, -\theta)$, leading that J_1 is θ -even and J_0 is θ -odd. This also agrees with the results in Eqs. (43-46).

VI. DISCUSSION

As discussed in Sec. IV A, utilizing a circularly polarized two-frequency drive enables the directional separation of shift and injection photocurrents, allowing for the separate detection of these two types of photocurrents. From Eqs. (35,36) with $(\varepsilon_1, \varepsilon_2) = (1, -1)$, their ratio is given by

$$\frac{J_1^z}{J_0^x} = \frac{\eta^2(7 + \eta^2) \hbar\Omega}{23 + 41\eta^2 \gamma_0} = \frac{\eta^2(7 + \eta^2)}{23 + 41\eta^2} \tau\Omega \quad (63)$$

and determined by the ratio of the input frequency Ω to the system's relaxation rate γ_0 . This is because J_1 and J_0 have different powers for the low-frequency divergence. Inserting the typical parameters, $\hbar\Omega = 0.1$ eV and $\tau = \hbar/\gamma_0 = 1$ ps, we obtain

$$\frac{J_1^z}{J_0^x} \sim \frac{15\eta^2(7 + \eta^2)}{23 + 41\eta^2} \quad (64)$$

For the typical example of a Dirac semimetal, Cd_3As_2 , where $\eta \approx 1/4$, it can be seen that the magnitude of J_1 and J_0 are comparable as $J_1^z/J_0^x \sim 0.26$.

In 3D Dirac systems, the estimated magnitude of the third-order photocurrent density is approximately $J_1^{3D} \sim 10^6$ A/m², adopting realistic parameters, $\hbar\Omega = 0.1$ eV, $E_0 = 1$ kV/cm, $v_F = 10^6$ m/s, and $\tau = \hbar/\gamma_0 = 1$ ps. For a sample with a width of $L = 100$ μm and a penetration depth of $\delta = 1$ μm , the magnitude of the photocurrent is estimated to be $I^{3D} = J_1^{3D} L \delta \sim 100$ μA , indicating that a large photocurrent is expected under a two frequency drive in the mid-infrared region. The substantial enhancement in J is caused by the low-frequency divergence of the conductivities due to the gapless nature of Dirac semimetals, as suggested in sections IV and V A. In contrast, for a two-dimensional (2D) Dirac system like graphene, the current density is given by

$$J_1^{2D} \sim J_1^{3D} \frac{v_F}{\Omega}. \quad (65)$$

Hence, the photocurrent is estimated to be $I^{2D} = J_1^{2D} L \sim 1$ μA , which is also large enough to be observed experimentally. These large photocurrent responses in gapless systems using a two-frequency drive provide a new venue to the dynamic control of photocurrents with possible applications in optoelectronic devices in the mid-infrared or terahertz range.

ACKNOWLEDGMENTS

This work was supported by JSPS KAKENHI Grant 20K14407 (S.K.), 23K25816, 23K17665, 24H02231 (T.M.), and JST CREST (Grant No. JPMJCR19T3) (S.K., T.M.). Y.I. was supported by JSPS fellowship (No.24KJ0731).

-
- [1] P. J. Sturman and V. M. Fridkin, "Photovoltaic and Photo-refractive Effects in Noncentrosymmetric Materials," **CRC Press, Philadelphia** **8** (1992).
- [2] I. Grinberg, D. V. West, M. Torres, G. Gou, D. M. Stein, L. Wu, G. Chen, E. M. Gallo, A. R. Akbashev, P. K. Davies, J. E. Spanier, and A. M. Rappe, "Perovskite oxides for visible-light-absorbing ferroelectric and photovoltaic materials," **Nature** **503**, 509 (2013).
- [3] W. Nie, H. Tsai, R. Asadpour, J.-C. Blancon, A. J. Neukirch, G. Gupta, J. J. Crochet, M. Chhowalla, S. Tretiak, M. A. Alam, H.-L. Wang, and A. D. Mohite, "High-efficiency solution-processed perovskite solar cells with millimeter-scale grains," **Science** **347**, 522 (2015).
- [4] L. Z. Tan, F. Zheng, S. M. Young, F. Wang, S. Liu, and A. M. Rappe, "Shift current bulk photovoltaic effect in polar materials—hybrid and oxide perovskites and beyond," **npj Comput. Mat.** **2** (2016).
- [5] Z. Dai and A. M. Rappe, "Recent progress in the theory of bulk photovoltaic effect," **Chem. Phys. Rev.** **4**, 011303 (2023).
- [6] N. Nagaosa and T. Morimoto, "Concept of Quantum Geometry in Optoelectronic Processes in Solids: Application to Solar Cells," **Adv. Mater.** **29**, 1603345 (2017).
- [7] J. Orenstein, J. Moore, T. Morimoto, D. Torchinsky, J. Harter, and D. Hsieh, "Topology and Symmetry of Quantum Materials via Nonlinear Optical Responses," **Ann. Rev. Condens. Matter Phys.** **12**, 247 (2021).
- [8] T. Wehling, A. Black-Schaffer, and A. Balatsky, "Dirac materials," **Adv. Phys.** **63**, 1–76 (2014).
- [9] M. Neupane, S.-Y. Xu, R. Sankar, N. Alidoust, G. Bian, C. Liu, I. Belopolski, T.-R. Chang, H.-T. Jeng, H. Lin, A. Bansil, F. Chou, and M. Z. Hasan, "Observation of a three-dimensional topological Dirac semimetal phase in high-mobility Cd_3As_2 ," **Nat. Commun.** **5**, 3786 (2014).
- [10] Z. K. Liu, J. Jiang, B. Zhou, Z. J. Wang, Y. Zhang, H. M. Weng, D. Prabhakaran, S.-K. Mo, H. Peng, P. Dudin, T. Kim, M. Hoesch, Z. Fang, X. Dai, Z. X. Shen, D. L. Feng, Z. Hussain, and Y. L. Chen, "A stable three-dimensional topological Dirac semimetal Cd_3As_2 ," **Nat. Mater.** **13**, 677 (2014).
- [11] Z. K. Liu, B. Zhou, Y. Zhang, Z. J. Wang, H. M. Weng, D. Prabhakaran, S.-K. Mo, Z. X. Shen, Z. Fang, X. Dai, Z. Hussain, and Y. L. Chen, "Discovery of a three-dimensional topological Dirac semimetal, Na_3Bi ," **Science** **343**, 864 (2014).
- [12] K. S. Novoselov, A. K. Geim, S. V. Morozov, D. Jiang, M. I. Katsnelson, I. V. Grigorieva, S. V. Dubonos, and A. A. Firsov, "Two-dimensional gas of massless Dirac fermions in

- graphene," *Nature* **438**, 197–200 (2005).
- [13] H. Zhang, C.-X. Liu, X.-L. Qi, X. Dai, Z. Fang, and S.-C. Zhang, "Topological insulators in Bi_2Se_3 , Bi_2Te_3 and Sb_2Te_3 with a single Dirac cone on the surface," *Nat. Phys.* **5**, 438–442 (2009).
- [14] A. A. Burkov, "Chiral anomaly and transport in Weyl metals," *Journal of Physics: Condensed Matter* **27**, 113201 (2015).
- [15] T. Morimoto and N. Nagaosa, "Chiral Anomaly and Giant Magnetochiral Anisotropy in Noncentrosymmetric Weyl Semimetals," *Phys. Rev. Lett.* **117**, 146603 (2016).
- [16] T. Morimoto, S. Zhong, J. Orenstein, and J. E. Moore, "Semi-classical theory of nonlinear magneto-optical responses with applications to topological Dirac/Weyl semimetals," *Phys. Rev. B* **94**, 245121 (2016).
- [17] C.-K. Chan, N. H. Lindner, G. Refael, and P. A. Lee, "Photocurrents in Weyl semimetals," *Phys. Rev. B* **95**, 041104 (2017).
- [18] O. Matsyshyn, F. Piazza, R. Moessner, and I. Sodemann, "Rabi Regime of Current Rectification in Solids," *Phys. Rev. Lett.* **127**, 126604 (2021).
- [19] J. Ahn, G.-Y. Guo, and N. Nagaosa, "Low-Frequency Divergence and Quantum Geometry of the Bulk Photovoltaic Effect in Topological Semimetals," *Phys. Rev. X* **10**, 041041 (2020).
- [20] F. de Juan, A. G. Grushin, T. Morimoto, and J. E. Moore, "Quantized circular photogalvanic effect in Weyl semimetals," *Nat. Commun.* **8**, 15995 (2017).
- [21] R. Atanasov, A. Haché, J. L. P. Hughes, H. M. van Driel, and J. E. Sipe, "Coherent Control of Photocurrent Generation in Bulk Semiconductors," *Phys. Rev. Lett.* **76**, 1703 (1996).
- [22] J. Rioux and J. Sipe, "Optical injection processes in semiconductors," *Physica E: Low-dimensional Systems and Nanostructures* **45**, 1 (2012).
- [23] Y. Ikeda, S. Kitamura, and T. Morimoto, "Photocurrent Induced by a Bircircular Light Drive in Centrosymmetric Systems," *Phys. Rev. Lett.* **131**, 096301 (2023).
- [24] D. A. Bas, K. Vargas-Velez, S. Babakiray, T. A. Johnson, P. Borisov, T. D. Stanescu, D. Lederman, and A. D. Bristow, "Coherent control of injection currents in high-quality films of Bi_2Se_3 ," *Appl. Phys. Lett.* **106**, 041109 (2015).
- [25] O. Neufeld, D. Podolsky, and O. Cohen, "Floquet group theory and its application to selection rules in harmonic generation," *Nat. Commun.* **10**, 405 (2019).
- [26] O. Kfir, P. Grychtol, E. Turgut, R. Knut, D. Zusin, D. Popmintchev, T. Popmintchev, H. Nembach, J. M. Shaw, A. Fleischer, H. Kapteyn, M. Murnane, and O. Cohen, "Generation of bright phase-matched circularly-polarized extreme ultraviolet high harmonics," *Nat. Photonics* **9**, 99 (2015).
- [27] K. Ogawa, N. Kanda, Y. Murotani, and R. Matsunaga, "Programmable generation of counterrotating bircircular light pulses in the multi-terahertz frequency range," *arXiv:2312.04768* (2023).
- [28] T. Nag, R.-J. Slager, T. Higuchi, and T. Oka, "Dynamical synchronization transition in interacting electron systems," *Phys. Rev. B* **100**, 134301 (2019).
- [29] M. S. Mrudul, Álvaro Jiménez-Galán, M. Ivanov, and G. Dixit, "Light-induced valleytronics in pristine graphene," *Optica* **8**, 422 (2021).
- [30] T. V. Trevisan, P. V. Arribi, O. Heinonen, R.-J. Slager, and P. P. Orth, "Bircircular Light Floquet Engineering of Magnetic Symmetry and Topology and Its Application to the Dirac Semimetal Cd_3As_2 ," *Phys. Rev. Lett.* **128**, 066602 (2022).
- [31] K. Sandholzer, A.-S. Walter, J. Minguzzi, Z. Zhu, K. Viebahn, and T. Esslinger, "Floquet engineering of individual band gaps in an optical lattice using a two-tone drive," *Phys. Rev. Res.* **4**, 013056 (2022).
- [32] J. Minguzzi, Z. Zhu, K. Sandholzer, A.-S. Walter, K. Viebahn, and T. Esslinger, "Topological Pumping in a Floquet-Bloch Band," *Phys. Rev. Lett.* **129**, 053201 (2022).
- [33] N. Rana, M. S. Mrudul, and G. Dixit, "Generation of Circularly Polarized High Harmonics with Identical Helicity in Two-Dimensional Materials," *Phys. Rev. Appl.* **18**, 064049 (2022).
- [34] Y. Ikeda, S. Kitamura, and T. Morimoto, "Floquet engineering of electric polarization with two-frequency drive," *Prog. Theor. Exp. Phys.* **2022**, 04A101 (2022).
- [35] Y. Wang, A.-S. Walter, G. Jotzu, and K. Viebahn, "Topological Floquet engineering using two frequencies in two dimensions," *Phys. Rev. A* **107**, 043309 (2023).
- [36] R. D. R. Bhat and J. E. Sipe, "Optically Injected Spin Currents in Semiconductors," *Phys. Rev. Lett.* **85**, 5432 (2000).
- [37] J. Rioux, J. E. Sipe, and G. Burkard, "Interference of stimulated electronic Raman scattering and linear absorption in coherent control," *Phys. Rev. B* **90**, 115424 (2014).
- [38] R. A. Muniz and J. E. Sipe, "Coherent control of optical injection of spin and currents in topological insulators," *Phys. Rev. B* **89**, 205113 (2014).
- [39] Z. Zheng, Y. Song, Y. W. Shan, W. Xin, and J. L. Cheng, "Optical coherent injection of carrier and current in twisted bilayer graphene," *Phys. Rev. B* **105**, 085407 (2022).
- [40] D. E. Parker, T. Morimoto, J. Orenstein, and J. E. Moore, "Diagrammatic approach to nonlinear optical response with application to Weyl semimetals," *Phys. Rev. B* **99**, 045121 (2019).
- [41] A. A. Soluyanov, D. Gresch, Z. Wang, Q. Wu, M. Troyer, X. Dai, and B. A. Bernevig, "Type-II Weyl semimetals," *Nature* **527**, 495 (2015).
- [42] M. Hirayama, R. Okugawa, S. Ishibashi, S. Murakami, and T. Miyake, "Weyl Node and Spin Texture in Trigonal Tellurium and Selenium," *Phys. Rev. Lett.* **114**, 206401 (2015).
- [43] F. Flicker, F. de Juan, B. Bradlyn, T. Morimoto, M. G. Vergniory, and A. G. Grushin, "Chiral optical response of multifold fermions," *Phys. Rev. B* **98**, 155145 (2018).